Accepted Manuscript

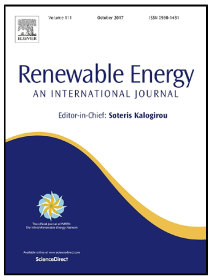

Investigations of unsteady pressure loading in a Francis turbine during variable-speed operation

Chirag Trivedi, Einar Agnalt, Ole Gunnar Dahlhaug

PII: S0960-1481(17)30506-2

DOI: 10.1016/j.renene.2017.06.005

Reference: RENE 8869

To appear in: *Renewable Energy*

Received Date: 01 March 2017

Revised Date: 29 May 2017

Accepted Date: 01 June 2017

Please cite this article as: Chirag Trivedi, Einar Agnalt, Ole Gunnar Dahlhaug, Investigations of unsteady pressure loading in a Francis turbine during variable-speed operation, *Renewable Energy* (2017), doi: 10.1016/j.renene.2017.06.005

Investigations of unsteady pressure loading in a Francis turbine during variable-speed operation

Chirag Trivedi[1]

Postdoctoral Fellow, Waterpower Laboratory, Norwegian University of Science and Technology, Norway.

Einar Agnalt

Ph. D. candidate, Waterpower Laboratory, Norwegian University of Science and Technology, Norway.

Ole Gunnar Dahlhaug

Professor, Waterpower Laboratory, Norwegian University of Science and Technology, Norway.

ABSTRACT

Current study was aimed to investigate the unsteady pressure loading in a model Francis turbine under variable-speed configurations. Focus was to investigate the time-dependent characteristic frequencies and the pressure amplitudes. Detailed analysis of both stochastic and deterministic pressure loading in the vaneless space, runner and draft tube was conducted. Total 12 pressure sensors were integrated in the turbine, including four sensors in the runner. The runner rotational speed was changed by ±30% of the rated speed, and the guide vanes were at a fixed aperture. Total four operating conditions were investigated. The measurements showed that, in the vaneless space and runner, amplitudes of unsteady pressure fluctuations increase with the runner angular speed. Pressure field at the blade trailing edge is strongly influenced by the draft tube flow at part load and low load. The variable-speed configuration allowed power generation under the stable condition, where the vortex rope effect is low. However, this led to high-amplitude stochastic frequencies in the runner and draft tube. Overall, the pressure measurements indicated that not only efficiency but also detailed study on pressure fluctuations inside the turbine is vital before designing a runner for the variable-speed configurations.

Keywords: design; Francis turbine; hydropower; pressure; renewable energy; variable-speed

1. Introduction

Electricity demand of a country is met by both continual and intermittent types of energy sources [1, 2]. Hence, any variation in the intermittent energy source can affect the grid network and the other base load turbines [3]. To compensate such variation, counter balance is needed, which is provided by the hydraulic turbines [4, 5]. Because, the base load units (continual type) respond slowly against the load change, and the power generation cost is high. The hydraulic turbines provide flexibility of real-

[1]Postal address: Department of Energy and Process Engineering, Norwegian University of Science and Technology (NTNU), NO-7491 Trondheim, Norway. Tel: +47 735 93849. E-mail: chirag.trivedi@ntnu.no

time load change according to the demand [6]. The turbines respond quickly (less than a second) using synthetic inertia control to primary (few seconds), secondary (less than a minute) and territory (few minutes) controls depending on the requirement [7-9]. During low demand, the turbines are operated at the minimum load or speed-no-load (SNL), which allows energy storage [10-13].

Francis type hydraulic turbines are the most common in use today. The turbines are operated at the fixed rotational speed governed by the grid frequency of a country [14]. Traditionally, Francis turbines are designed for a fixed speed and a variable discharge characteristics. Hence, the mechanical power from a runner is managed by the guide vane aperture (discharge control). Such turbines work well at the design point, i.e., best efficiency point (BEP), and the turbine efficiency is high. However, when the electricity demand is low/high, the turbines are forced to operate under off-design condition, and the turbines experience fatigue due to high amplitude pressure fluctuations, vortex breakdown and cavitation [15]. Extensive studies have been conducted to investigate the problems during the last three decades, but it is far from the realistic solutions [16-21]. Variable-speed configuration may be a better alternative to improve dynamic stability of the turbines.

Turbines are designed for one of three approaches: (1) low flexibility- fixed speed and discharge, (2) medium flexibility- fixed speed and variable discharge, and (3) high flexibility- variable speed and discharge [5, 22, 23]. The first approach is used for run of river power plant, where guide vanes are fixed permanently (or no guide vanes) to reduce the operating/maintenance cost. Such turbines are not applicable to meet the real-time demand. The second approach is widely used due to high efficiency and low cost [24]. However, such turbines experience dynamic instability when they are operated at the off-design load [15, 17, 25]. The third approach provides moderate to high flexibility to meet real-time demand and stabilize the power grid when wind/solar power fluctuates rapidly [26, 27]. Advantage of this approach is the flexibility of two variables, i.e., rotational speed and discharge, which enables a wide range of power output and two different combinations for the same load. Thus, dynamic stability can be maintained unlike the second approach.

Currently, variable-speed technology is integrated either retrofitting in the existing turbines or designing a completely new turbine. Retrofitting allows cost saving, but the flow field during the speed variation is not known clearly [28]. Pressure measurements in a Francis turbine showed that the amplitudes of unsteady pressure fluctuations are high in the runner during speed variation [29-32]. The amplitudes were strongly associated with the instantaneous rotational speed of the runner. During speed variation, complex pressure field is developed in the vaneless space due to constant change of runner tangential velocity. Similarly, in the blade passages, swirls are developed as the runner speed changes, which further increase the flow instability and cause high amplitude pressure fluctuations [33-35]. In the Francis turbines, the main challenge is the high amplitude dynamic stresses from the rotor-stator interaction (RSI) [36]. The dynamic stresses cause fatigue and crack to the runner blades [37-39]. Sometimes, the stresses induce crack within few months of turbines operation [40, 41].

The variable-speed characteristic allows turbines to adjust the rotational speed independent from the grid frequency. The problems at off-design load can be reduced without significantly reducing the turbine efficiency [26]. The turbine can be operated under a stable operating region for the same load. Very few studies on the variable-speed characteristics have been conducted, and most of them focused on the global parameters, such as efficiency improvement, head and speed variations [1, 2, 5, 9, 27, 42, 43].

So far majority of studies are focused on constant speed (i.e., synchronous) and discharge (fixed guide vane opening) conditions, where the frequencies of unsteady pressure fluctuations are nearly constant. The pressure amplitudes are dependent on the operating load. Expected frequencies and the amplitudes are well predicted along with the hill diagram of a model/prototype turbine during model test. But the turbine designs are currently inclined towards variable-speed to improve the power grid stability [9], where the runner rotational speed is not constant. In this situation, characteristic frequencies and the pressure amplitudes are no longer constant and those vary with the rotational speed. State of the art studies under such conditions indicated that the composition of deterministic and stochastic frequencies vary with the rotational speed. At certain locations in the turbine, amplitudes of stochastic component of frequencies may cause heavy fatigue loading to the blades [44]. Detailed investigation of unsteady pressure loading is essential to understand the characteristic frequencies and flow field during the speed variation and to make robust design of the future turbines.

The present work is aimed to investigate the amplitudes of unsteady pressure fluctuations at different locations inside the turbine during speed variation and to investigate the change of pressure amplitudes with load. The measurements were conducted on a high head model Francis turbine for different guide vane apertures (GVA) starting from a minimum load to the full load. To account for the extreme scenario, runner rotational speed was changed up to 30% of the rated speed. The GVA was fixed during the speed variation. Flush mount pressure sensors were integrated in the vaneless space, runner and draft tube to acquired unsteady pressure data. Current study showed that both characteristic frequencies and amplitudes are strongly dependent on the runner rotational speed and corresponding discharge. Around the rated speed (±10%), amplitudes of deterministic frequencies are dominant. Away from the rated speed (±20-30%), amplitudes of stochastic frequencies were high, particularly at the blade trailing edge and the draft tube. The frequencies were seen in the range of 10-50 Hz and 170-250 Hz.

2. Francis turbine

Test rig available at the Waterpower Laboratory, Norwegian University of Science and Technology (NTNU) was used for the measurements. The test rig is capable of operating under two different configurations, close loop and open loop, according to the measurement types. The close loop is preferred for steady-state measurements, and the open loop is preferred for transient measurements. The open loop provides identical configurations to the prototype during speed/discharge variations [45]. Figure 1 shows open loop configuration. Water from the large reservoir (9) is continuously pumped to the overhead tank (2) and flowed down (gravity) to the turbine (7). The overhead tank acts as a reservoir. Discharge to the turbine is regulated by the guide vanes. The feed pumps (1) can be operated at the selected speed to obtain a required head for the measurements. There are two pumps, each driven by 315 kW variable-speed motor, and the pumps can be operated in either series or parallel depending on discharge/head requirements. The draft tube outlet is connected to a downstream tank (8), where a constant water level is maintained at an atmospheric pressure, and the water above runner centerline is discharged to the basement (9). The open loop can produce a head up to 16 m, and the close loop can produce a head up to 100 m (discharge up to 0.5 m^3 s^{-1}). For the current measurements, open loop was used, which enabled configurations similar to a prototype. The turbine is a reduced scale (1:5.1) model of a prototype operating at Tokke power plant, Norway. The turbine includes 14 stay vanes integrated inside the spiral casing, 28 guide vanes, a runner with 15 full-length blades and 15 splitters, and a draft tube. The runner inlet and outlet diameters are 0.63 and 0.347 m, respectively. The Reynolds number is 1.87×10^6 at the BEP. The runner and DC generator rotor are coupled on the same shaft. The DC generator-motor was always connected to the load during the measurements.

For the variable-speed measurements, a LabView program was developed and integrated into the governing system for the speed control. The frequency response time of the pressure sensors was much higher than the data logging rate. The frequency response time of the magnetic flowmeter was very low (1 Hz) therefore time dependent discharge variation is not discussed in the article. In this turbine, discharge variation is inversely proportional to the runner rotational speed for fixed GVA.

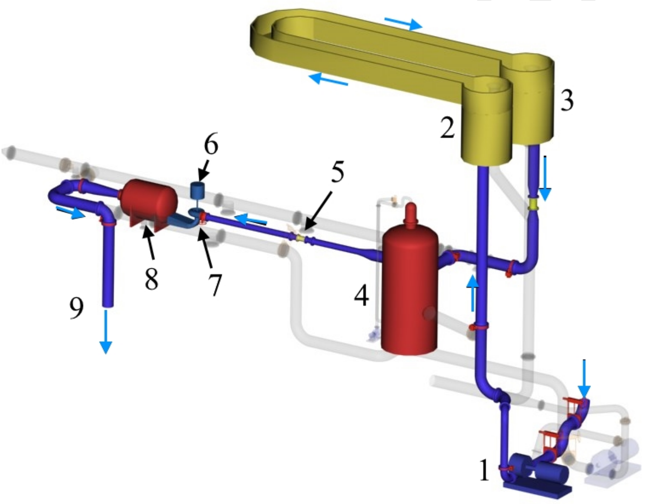

Figure 1 Open loop hydraulic system at the Waterpower Laboratory, NTNU. (1) feed pump (2) overhead tank-primary, (3) overhead tank-secondary, (4) pressure tank, (5) magnetic flowmeter, (6) DC generator, (7) Francis turbine, (8) downstream tank and (9) basement.

The Francis turbine was equipped with all required instruments to conduct model testing according to IEC 60193 [46]. Additional 10 pressure sensors were flush mounted at different locations in the turbine and their locations are shown in Figure 2. Two sensors (VL1 and VL2) are in the vaneless space; four sensors (R1, R2, R3 and R4) are on the runner crown, between two blades; four sensors (DT1, DT2, DT3, and DT4) are on the wall of the draft tube cone. Two additional sensors (IN1 and IN2) are mounted at the turbine inlet conduit to monitor water hammer. Calibration and uncertainty quantification of all measuring instruments and sensors were conducted. IEC 60193 [46] was followed for quantifying the uncertainties in the turbine efficiency. The uncertainties obtained from the calibration are listed in Table 1. The total uncertainty ($\hat{e}_t$) of ±0.2% includes both systematic and random uncertainties (see Equation (2)). The systematic uncertainty is the root-sum-square of the uncertainties in discharge ($\hat{e}_Q$), head ($\hat{e}_H$), torque ($\hat{e}_T$) and runner rotational speed ($\hat{e}_n$) from the calibration. The maximum uncertainties of the pressure sensors located in the vaneless space, runner and draft tube were ±0.12, ±0.26 and ±0.14%, respectively. Uncertainty in the guide vane angular positioning ($\hat{e}_\alpha$) was ±0.7%.

$$\hat{e}_s = \pm\sqrt{\hat{e}_Q^2 + \hat{e}_H^2 + \hat{e}_T^2 + \hat{e}_n^2 + \hat{e}_\rho^2} \tag{1}$$

$$\hat{e}_t = \pm\sqrt{\hat{e}_s^2 + \hat{e}_r^2}\ ; \tag{2}$$

where $\hat{e}_s$ and $\hat{e}_r$ are the systematic and random uncertainties in percentage.

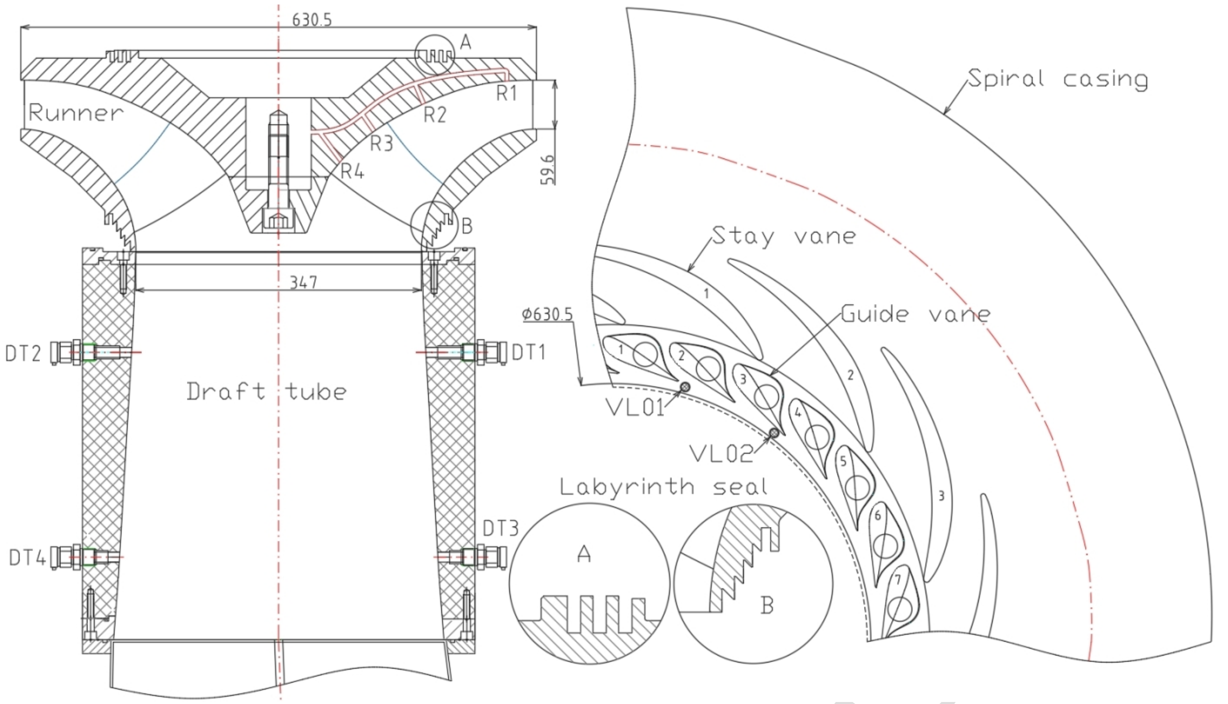

Figure 2 Locations of pressure sensors in the turbine. Sensors R1, R2, R3 and R4 are in the runner; DT1, DT2, DT3 and DT4 are in the draft tube cone; VL1 and VL2 are in the vaneless space.

Table 1 Computed uncertainties in the flow measurement through calibration.

$\hat{e}_H$	$\hat{e}_Q$	$\hat{e}_T$	$\hat{e}_n$	$\hat{e}_\rho$	$\hat{e}_r$	$\hat{e}_t$	$\hat{e}_{VL}$	$\hat{e}_R$	$\hat{e}_{DT}$	$\hat{e}_\alpha$
±0.17	±0.12	±0.15	±0.035	±0.01	±0.18	±0.2	±0.12	±0.26	±0.14	±0.7

To determine the repeatability of the test rig, measurements were conducted at steady-state BEP, high load, part load and minimum load before the current measurements. The results were compared with available benchmark data [47, 48], and the maximum deviation was within the uncertainty ($\hat{e}_r$) limit. The BEP was obtained at α=9.9°, n_{ED}=0.18, Q_{ED}=0.15, and the hydraulic efficiency was 93.1±0.2%.

$$n_{ED} = \frac{nD}{\sqrt{E}} \quad (\text{-}), \tag{3}$$

$$Q_{ED} = \frac{Q}{D^2\sqrt{E}} \quad (\text{-}); \tag{4}$$

where n is the runner rotational speed in revolutions per second, D is the runner reference dimeter in m, E is the specific hydraulic energy in J kg^{-1} and Q is the turbine inlet discharge in m^3 s^{-1}.

The pressure data were analyzed for all transient conditions. The data were acquired at a sampling rate of 5 kHz. Slip-ring mechanism was used to acquire data from the runner sensors. Natural frequencies of the pressure sensors were above 25 kHz. Detailed pressure measurements on the turbine were conducted and key findings are discussed to avoid unnecessary repetition of the same flow phenomena.

3. Results and discussions

3.1 Global variation

Experiments were conducted for four different GVA, i.e., 8, 70, 100 and 140%, and 2 cases of speed variation, i.e., runner speed increase and decrease, for each GVA. The GVA of 8 and 140% correspond to the minimum and maximum load in the turbine, respectively. The GVA of 70% corresponds to the part load, where the amplitudes of vortex rope are maximum. Variation of the runner rotational speed was ±100 rpm (n_{ED}=±0.05), which is equivalent to ±30% of the rated speed. In addition to the pressure data, torque, rotational speed, friction torque and net head were acquired during the speed variation.

The torque and power values during the speed variation at 100% GVA are shown in Figure 3. Time t=0 s represents start time of the load change (throughout the paper). Before t=0 s, the turbine was operating at the steady load. The flow parameters are normalized by the corresponding steady value ($x_{t=0}$),

$$x^* = \frac{x(t)}{x_{t=0}} \quad (\text{-})\,. \tag{5}$$

As shown in Figure 3(a), 100% GVA, the speed is increased linearly, and the load is ramping up at a rate of 9% per second. The speed is increased by 100 rpm during 0-2.5 s, and total power output ($P=T\omega$) is increased by 22%. The torque is reducing by an approximately same rate because discharge is reduced. In this turbine, discharge is inversely proportional to the runner speed. Power is proportional to the runner angular speed (ω) for the constant GVA. The opposite variation can be seen for the speed reduction case in Figure 3(b), except power. The power increases for the few moments, 0-0.5 s, and then decreases. This may be due to the dominant effect of mechanical inertia (flywheel effect). The flywheel effect is sometimes very useful to stabilize the power grid [14]. In the hydraulic turbines, the flywheel effect is low as compared to the other base load turbines, such as thermal, nuclear and gas turbines. For a prototype, flywheel effect is estimated at the time of commissioning using runner acceleration (ω), polar moment of inertia of the rotating masses (J) and torque (T).

$$t_{\text{start}} = \frac{J\omega}{T} \quad \text{(s)} \tag{6}$$

The flywheel effect is limited by the allowed speed range and the maximum possible torque delivered by a turbine [43]. Therefore, in some cases, ideal response time may be slower than the expected. The mechanical start time is dependent on the flywheel effect (GD^2) of the rotating masses, runner acceleration (ω^2) and power (P),

$$t_m = \frac{GD^2\omega^2}{P} \quad \text{(s)} \tag{7}$$

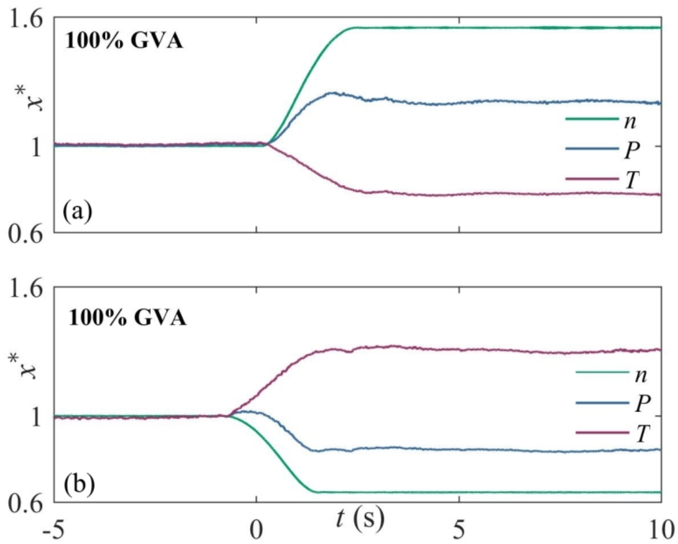

Figure 3 Variation of runner speed (n), power (P) and shaft torque (T) during speed variation at 100% GVA; t=0 s indicates the start time of speed change. The parameters are normalized with the corresponding initial steady value.

For all investigated cases, the trend of parameter variation was similar to the 100% GVA, except for 8% GVA. Time-dependent variation of the runner speed (n), power (P) and shaft torque (T) at 8% GVA is shown in Figure 4. Torque (also power) drops significantly (~200%) while increasing the runner speed (see Figure 4(a)), which is completely different from Figure 3(a). Large fluctuations in the torque value during speed variation correspond to switching from/to generator/motor mode to overcome the losses at that instant of time. The opposite variation can be seen for the case of speed decrease (Figure 4(b)). However, the generator/motor switching occurs at two points. Discharge to the runner at this GVA is extremely low, which may not be enough to meet the required torque value. Such condition is rare for the prototypes. Measurements at 8% GVA were conducted to investigate the extreme scenario in the turbine at very low discharge.

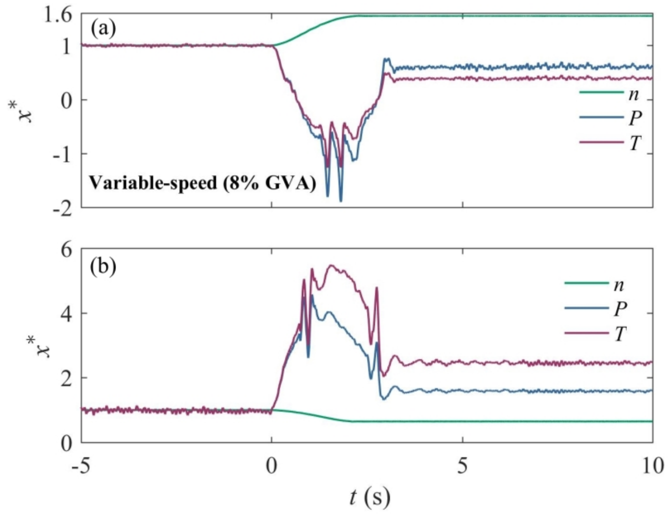

Figure 4 Variation of runner speed (n), power (P) and shaft torque (T) during speed variation at 8% GVA; t=0 s indicates the start time of speed change. The parameters are normalized with the corresponding initial steady value.

3.2 Characteristic frequencies

3.2.1 *Turbine inlet*

Two pressure sensors, IN1 and IN2, were flush mounted at the inlet conduit to acquire unsteady pressure fluctuations and water hammer during load change. The sensor IN2 was located at the spiral casing inlet. The sensor IN1 was located 7 m upstream from IN2. Pressure variation at IN1 and IN2 during power ramp-down at 100% GVA is shown in Figure 5. The pressure is normalized by the net head at BEP [47],

$$H^* = \frac{\left(\tilde{p}(t)/\rho g\right)}{H_{\mathrm{BEP}}} \quad (\text{-})\,; \qquad (8)$$

where $\tilde{p}(t)$ is the time-dependent pressure acquired during the measurements in Pa, ρ is the water density in kg m^{-3}, g is the gravity m s^{-2} and H_{BEP} is the net head at BEP in m. As runner speed decreases, pressure in the conduit drops rapidly due to increase of flow velocity. Total pressure drop is 3.2 and 3.4% at IN1 and IN2 locations, respectively. The pressure recovers slowly as flow stabilizes in the system. The frequency of oscillations is 0.35 Hz, which is dampened after 10 s. Instantaneous pressure fluctuations during load change are shown in Figure 6. Equation (9) [46] is used to normalize the pressure fluctuations. Factor of pressure fluctuations ($\tilde{p}_{\mathrm{E}}$),

$$\tilde{p}_{\mathrm{E}} = \frac{\tilde{p}(t) - \overline{p}(t)}{(\rho E)_{\mathrm{BEP}}} \quad (\text{-})\,; \tag{9}$$

where $\overline{p}(t)$ is the time-average pressure in Pa and other parameters are similar to those explained previously. Both high and low frequency fluctuations can be seen. The low frequency fluctuations are associated with the surging effect in the conduit. The high frequency fluctuations are associated with the blade passing frequency, which varies with the runner rotational speed (4.7-3.1 Hz), and the frequency of standing wave. After the speed variation, two dominating frequencies were obtained, e.g., the blade passing frequency of 92 Hz and the standing wave frequency of 42 Hz [49]. The pressure variation was similar for the other GVA, except the amplitudes of pressure fluctuations. For the 140% GVA, the pressure amplitudes were maximum, i.e., $\tilde{p}_{\mathrm{E}}$=1.2.

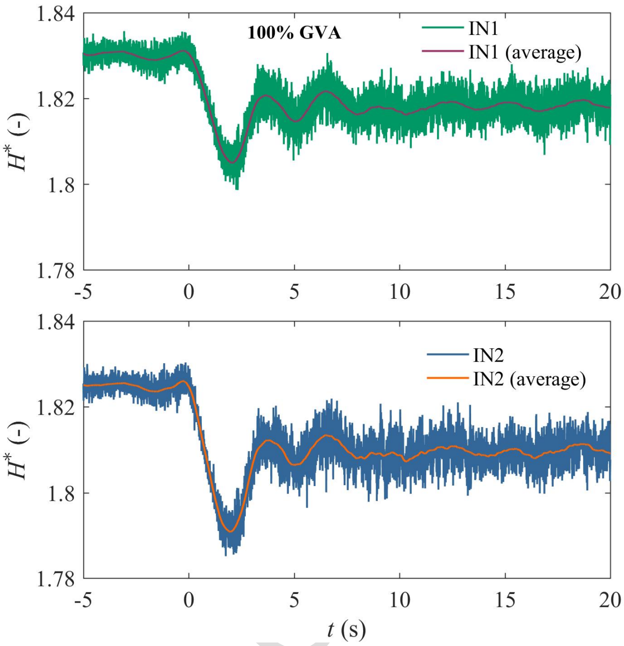

Figure 5 Unsteady pressure variation at the turbine inlet conduit during power ramp-down at 100% GVA. Time t=0 s is the start time of load change (or the runner speed change); H^* is computed using Equation (8).

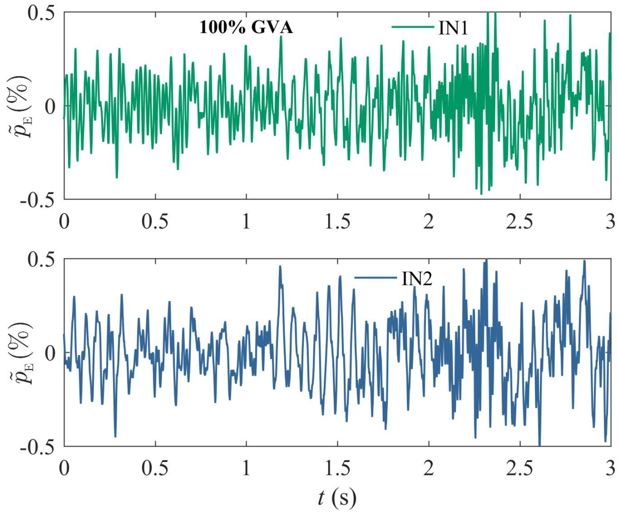

Figure 6 Factor of pressure fluctuations at the turbine inlet (IN1 and IN2) during power ramp-down at 100% GVA. $\tilde{p}_E$ is computed using Equation (9).

3.2.2 *Vaneless space*

To investigate the amplitudes of blade passing frequency, two pressure sensors (VL1 and VL2) were mounted in the vaneless space. A sensor VL1 was located at the trailing edge of a guide vane and VL2 was located before the trailing edge, where the vaneless space is minimum. Pressure fluctuations at VL1 during power ramp-down at 100% GVA are shown in Figure 7. Average pressure in the vaneless space is function of the runner rotational speed. However, the amplitudes of pressure fluctuations increase because operating point is moving away from the BEP. Gradual increase of pressure amplitudes can be clearly seen in Figure 7 (right). The high amplitude fluctuations correspond to the blade passing frequency (f_b), which is dependent on the runner rotational speed (n) and the number of blades (z_b),

$$f_b = nz_b \quad (\mathrm{Hz})\,. \tag{10}$$

Spectral analysis [50, 51] of the time-dependent pressure data was conducted to investigate the characteristic frequencies. Figure 8 shows the spectrogram of the unsteady pressure fluctuations at VL1 during power ramp-down at 100% GVA. The extracted pressure fluctuations ($\tilde{p}_E$) are also plotted (not scaled) in the same figure to visualize the amplitude variation. The blade passing frequency (f_b) decreases with the runner rotational speed and stabilized after 2.5 s. The frequency varies from 142 Hz to 92 Hz, and the root-mean-square amplitudes increases from 1.5 s. The variation of amplitudes is

0.8-0.9% of ρE. Random frequencies with the amplitudes of 0.7-0.8% of ρE are appeared as power reduces from BEP. Random fluctuations and the frequencies are described in section 3.3 Stochastic frequencies. At VL2 location, pressure amplitudes were similar to those obtained at VL1; however, the amplitudes of random frequencies were very low. This may be due to the location of the sensor, which is before the guide vane trailing edge and the effect of vortex shedding from the trailing edge was very low.

Trend of pressure variation for the other cases of variable-speed was similar to that presented in Figure 7. Variation in the pressure amplitudes was obtained. At 8% GVA, the amplitudes were low, and at 140% GVA, the amplitudes were maximum. Figure 9 shows the frequency spectrum at VL1 for 8% and 140% GVA cases. Both cases correspond to the power ramp-down. Amplitudes and frequencies are normalized using Equations (9) and (11), respectively.

$$f^* = \frac{f}{n} \quad (\text{-}); \tag{11}$$

where f is the frequency of pressure fluctuations in Hz and n is the runner rotational speed in revolutions per second. High amplitudes correspond to the blade passing frequency (f_b) in the vaneless space. Dimensionless frequency of 30 represents the number of blades in the runner. Three distinct frequencies are appeared, i.e., 15, 30 and 60. At 8% GVA, amplitudes of the blade passing frequency are decreased from 0.3% to 0.12% after the load reduction. However, at 140% GVA, the amplitudes are increased from 0.26% to 1%. Hence, speed reduction at 140% GVA may induce high-amplitude dynamic stresses on the blades. Flow field in the vaneless space is dependent on the available space between the runner and guide vanes, runner tangential velocity and discharge. For the current study, guide vanes are at constant position; therefore, influencing parameters are the rotational speed and the discharge. The runner tangential velocity decreased and the flow velocity increased due to increase of discharge. This has changed the flow angle approaching the runner blades and might resulted in flow instability, strong effect of vortex shedding from the guide vanes and enhanced fluid-structure interaction. Overall, at VL2 location, amplitudes of the blade passing frequency before and after the load change were 0.38% and 1.1 of ρE at 140% GVA respectively. The amplitudes are 0.1-0.15%

larger than those of VL1. This is because of reduced vaneless space at VL2 location as compared to the VL1. The locations of VL1 and VL2 can be seen in Figure 7. During RSI, reflection of the pressure waves is strong due to presence of guide vane wall near to VL2 sensor. At VL1, pressure waves can travel upstream through the guide vane passage and the reflection is weak.

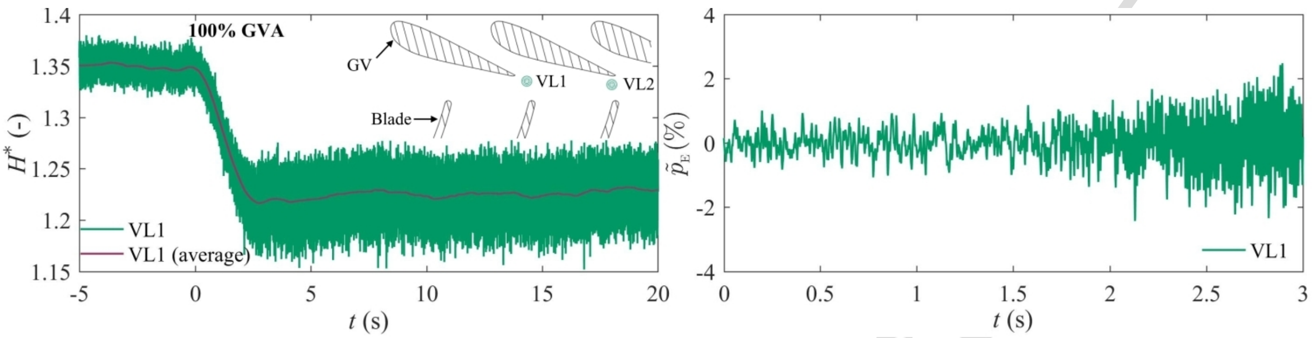

Figure 7 Pressure fluctuations in the vaneless space during power ramp-down at 100% GVA. Time t=0 s indicates the start time of speed reduction; VL1 and VL2 are the locations of pressure measurements in the vaneless space.

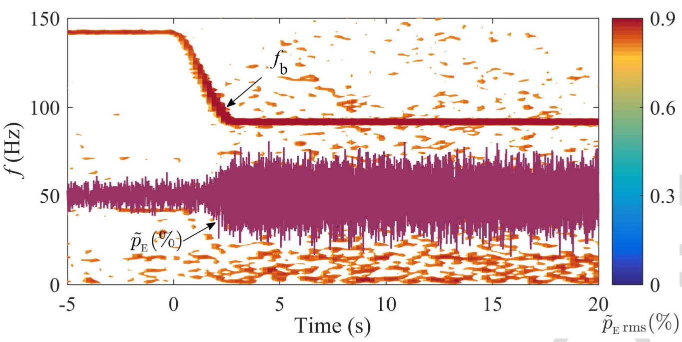

Figure 8 Spectrogram of the unsteady pressure fluctuations ($\tilde{p}_E$) acquired from VL1 during power ramp-down at 100% GVA. The scale of $\tilde{p}_E$ is same as shown in Figure 7 (right); Time t=0 s indicates the start time of speed reduction.

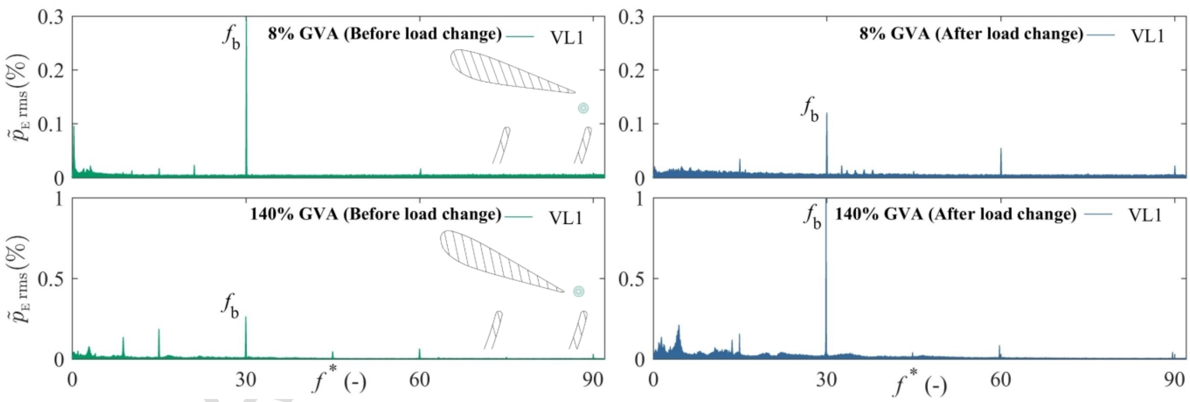

Figure 9 Frequency spectrum of pressure data at VL1 before and after the load change at 8 and 140% GVA. Y-axis scale is different for 8 and 140% GVA. The frequencies are normalized using Equation (11).

3.2.3 *Runner*

Interaction between the vortex shedding from the guide vane trailing edge and the location/size of the blade stagnation point is important in a high head Francis turbine. Size of the stagnation point varies with blade location as runner accelerates/decelerates. Moreover, flow leaving from the guide vane passages strikes to the blade leading edge at different angle and flow separation takes place due to mismatch of the inlet flow angle, which develops swirl at the runner inlet [35]. This may result of high-amplitude pressure fluctuations at the runner inlet. To investigate the pressure fluctuations in the runner, four pressure sensors were flush mounted on the crown. The runner includes 15 full-length blades and 15 splitters in alternate arrangement. Sensors R1 and R2 were located between a blade and a splitter. Sensors R3 and R4 were located between two blades, following the splitter trailing edge. Sensor R1 was at a distance of 10 mm from the runner inlet and the R4 was at a distance of 20 mm before the runner outlet edge. Sensors R2 and R3 were at equal distance from R1 and R4, respectively.

The pressure variation at R1, R2, R3 and R4 locations during power ramp-down at 100% GVA is shown in Figure 10. The pressure data are normalized by the net head at BEP (Equation (8)). Pressure at all locations decreases gradually as the runner angular speed drops. Pressure drop at R1 is approximately 25%, which is almost two times that of the VL1. Pressure drop at R2, R3 and R4 is 2-3%. Extracted pressure fluctuations ($\tilde{p}_{\mathrm{E}}$) at all locations are shown in Figure 11. Gradual increase of fluctuations can be seen at all the locations. Peak-to-peak amplitudes considering 2 s window at R1 are ~10% of ρE. At R2, R3 and R4 locations, the respective amplitudes are 5, 2.8 and 2.6% of ρE. The dominant RSI frequency in the pressure data is correspond to the guide vane passing (f_{gv}),

$$f_{\mathrm{gv}} = n z_{\mathrm{gv}} \quad (\mathrm{Hz})\,. \tag{12}$$

where z_{gv} is the number of guide vanes. Amplitude of the guide vane passing frequency gradually increased, which can be seen in Figure 12. The spectrograms show variations of frequencies and the corresponding amplitudes in time domain. The random noise below 0.1% of ρE is filtered out in the plot. Variation of the guide vane passing frequency (f_{gv}) can be seen clearly as runner speed decreased. The frequency varies from 132 Hz to 86 Hz. Before the load change, pressure amplitudes at R1, R2, R3 and R4 are 0.41%, 0.46%, 0.32% and 0.18% of ρE, respectively. After the load change, the respective amplitudes are 1.38%, 0.56%, 0.42%, 0.24% of ρE. As the runner angular speed deviates from the design point, stochastic fluctuations of wide range of frequencies started appearing, particularly at R2 and R4 locations. This may be attributed to the flow unsteadiness because R2 and R4 sensors were located near the trailing edge of the splitter and the blade, respectively. Flow separation and the strong swirling flow could result in stochastic noise in addition to the system vibration.

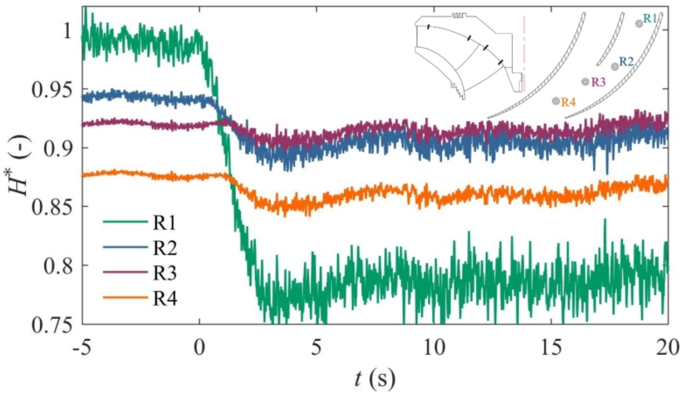

Figure 10 Pressure variation in the runner (R1, R2, R3 and R4) during power ramp-down at 100% GVA. Location R1 is 10 mm from the runner inlet and R4 is the 10 mm from the runner outlet. Pressure data are normalized by net head at BEP. Time t=0 s indicates the start time of speed reduction.

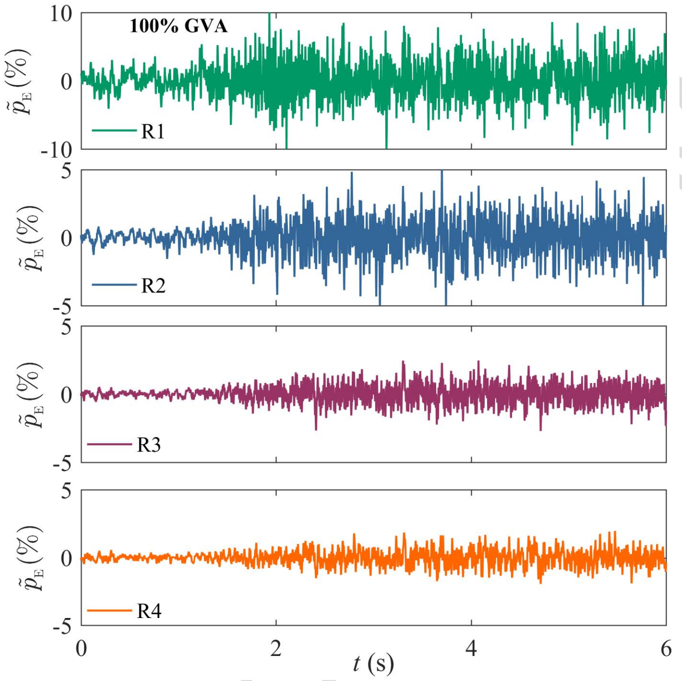

Figure 11 Extracted pressure fluctuations at R1, R2, R3 and R4 locations in the runner during power ramp-down at 100% GVA. Location R1 is 10 mm from the runner inlet and R4 is the 10 mm from the runner outlet; y-axis scale is different for R1. Time t=0 s indicates the start time of speed reduction.

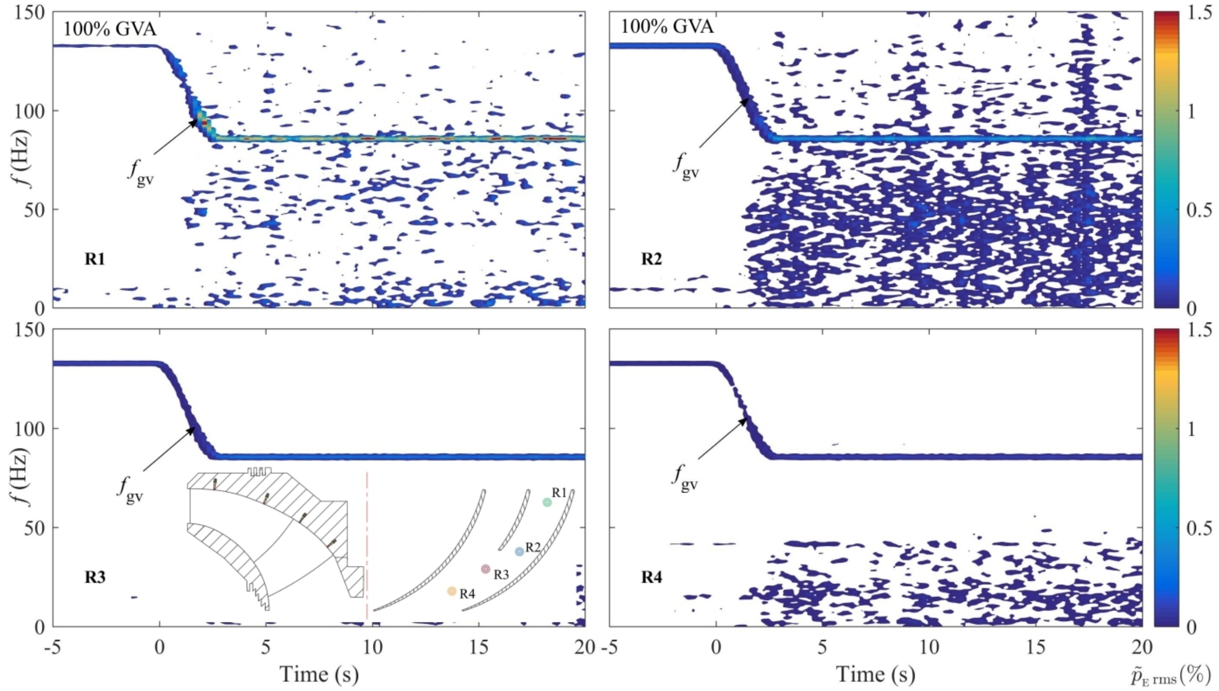

Figure 12 Spectrogram of the unsteady pressure fluctuations ($\tilde{p}_E$) acquired from runner locations (R1, R2, R3 and R4) during power ramp-down at 100% GVA. Time t=0 s indicates the start time of speed reduction.

Spectral analysis of the pressure data at R1 location for 8%, 70%, 100% and 140% GVA is shown in Figure 13. Left and right side plots show frequency spectrum before and after the power ramp-down, respectively. Pressure amplitudes and the frequencies and are normalized using Equations (9) and (11), respectively. At 8% GVA, amplitudes of the guide vane passing frequency decreased from 0.29% to 0.17%. At 100% and 140% GVA, variation of the pressure amplitudes is less than 10%, whereas, at 70% GVA, the amplitudes increased by 74% indicating the effect of RSI become stronger at this load. Harmonic ($0.5\times f_{gv}$) of the guide vane passing frequency at 140% GVA shows pressure amplitudes similar to the f_{gv}, and the first harmonic ($2\times f_{gv}$) shows 7% small amplitudes. Unexpectedly, frequency spectrum at 70% GVA shows a blade passing frequency. The blade passing frequency in the runner is rare occurrence. Detailed frequency analysis at 70% GVA is shown in Figure 14. A spectral analysis of the pressure data at R1, R2, R3 and R4 locations is shown. Amplitudes of the guide vane passing frequency decrease gradually from R1 to R4, but amplitudes of the blade passing frequency are remain constant at all the locations. This may be due to the hydro acoustic waves originated from RSI and travelling across the runner after reflecting from the either guide vanes or draft tube elbow.

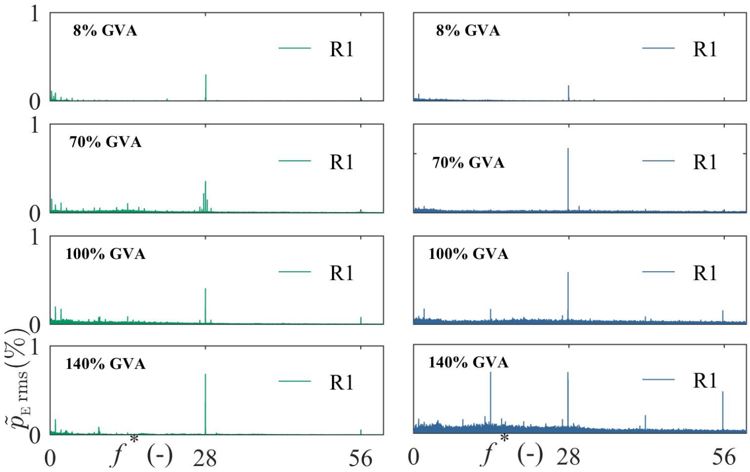

Figure 13 Spectral analysis of the pressure data obtained at R1 location in the runner before (left) and after (right) the power ramp-down at 8%, 70%, 100% and 140% GVA. The frequencies are normalized using Equation (11).

Time-dependent variation of both guide vane and the blade passing frequencies at R4 location can be seen in Figure 15. In addition to the guide vane passing frequency (f_{gv}), at time t=2 s, the blade passing frequency (f_b) is appeared. Difference between the blade passing frequency and the guide vane passing frequency is ~10 Hz. Amplitudes of the blade passing frequency are approximately 10% lower than that of the guide vane passing frequency. For a prototype turbine, small gap between the RSI frequencies may induce resonance in case of interference between the pressure waves [38, 52]. At 70% GVA and rated speed, the effect of vortex rope is dominant in the turbine. A frequency of vortex rope (f_{rh}) is obtained at R4 location, which can be clearly seen in the spectrogram before the load change. The frequency slowly disappeared as runner angular speed reduced further. Amplitudes of this frequency are very low as compared to the other deterministic frequencies originated from RSI. Further analysis of the draft tube flow is discussed in the following section.

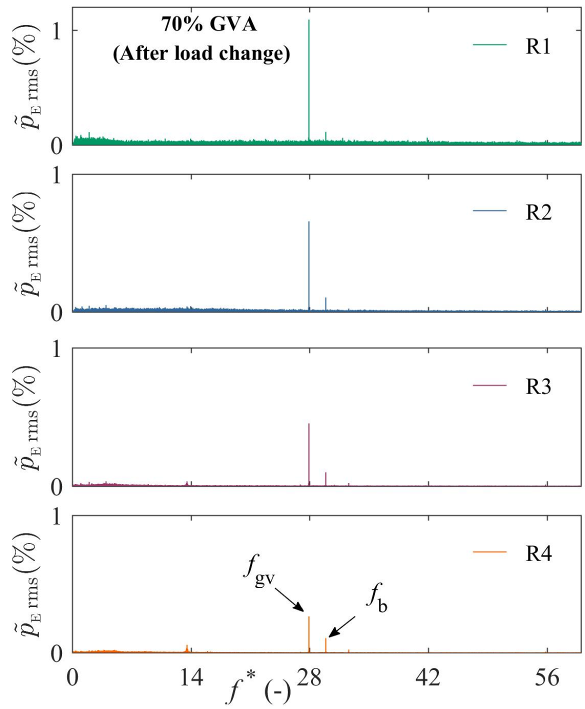

Figure 14 Spectral analysis of the pressure data acquired at 70% GVA after the load change. The frequencies are normalized using Equation (11).

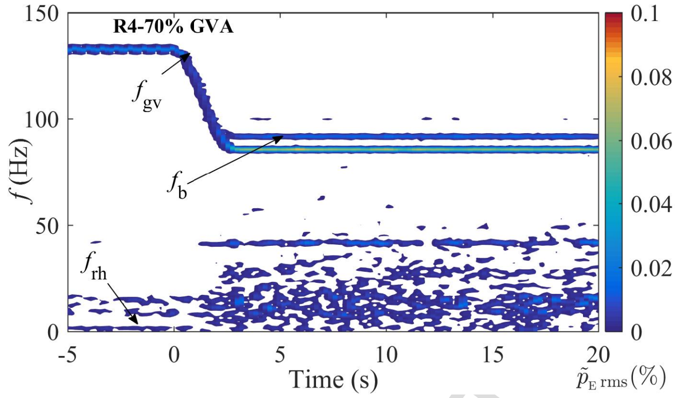

Figure 15 Spectrogram of the unsteady pressure fluctuations ($\tilde{p}_E$) acquired from runner location R4 during power ramp-down at 70% GVA. Time t=0 s indicates the start time of speed reduction.

3.2.4 *Draft tube*

Four piezoelectric (dynamic) type pressure sensors were integrated on the wall of the draft tube cone. Sensors DT1 and DT2 were located at 0.126 m from the runner outlet and 180° circumferentially apart from each other. DT3 and DT4 were located at 0.376 m from the runner outlet and 180° circumferentially apart from each other. The sensors were piezoelectric type therefore there was no absolute pressure measurements in the draft tube during the speed variations. Due to better dynamic properties of the sensors, accuracy towards amplitude and fluctuation measurements is high.

Flow field in the draft tube was different from that observed in the vaneless space and the runner during the load change. There was no significant pressure variation except large fluctuations and surging effect. Unsteady pressure fluctuations at DT1 for 8%, 70%, 100% and 140% GVA are shown in Figure 16. The pressure data are normalized using Equation (9). At 8% GVA, amplitudes of fluctuations are decreased after the load change (or speed reduction). However, at other GVA, the amplitudes are increased by up to three times from the initial value (before the load change). Peak-to-peak amplitudes are 0.5%, 1%, 2%, and 5% of ρE at 8%, 70%, 100% and 140% GVA, respectively. At 70% GVA, the turbine was operating at steady part load before the load change; where the pressure amplitudes were correspond to a vortex rope frequency (f_{rh}) of 1.67 Hz. After the load change, the vortex rope frequency was disappeared, but the stochastic fluctuations were increased significantly, which can be seen after 2.5 s. The amplitudes of the stochastic fluctuations were up to 0.9% of ρE. In addition, a frequency of blade passing was obtained with the amplitudes of approximately 0.3% of ρE. To investigate the frequency content in the pressure data acquired from the draft tube, spectral analysis was conducted, and Figure 17 shows frequencies at 8%, 70%, 100% and 140% GVA. The frequencies are shown for DT1 location in the draft tube. A dimensionless frequency of 30 is the blade passing frequency. A peak at f^*=16.3 and f^*=32.6 are the frequencies associated with the power grid frequencies, i.e., 50 Hz and 100 Hz. At 8% GVA, stochastic frequencies of low amplitudes are obtained in addition to the blade passing frequency (f_b). At 70% GVA, dominant amplitudes correspond to the blade frequency and the harmonic. At 100% GVA, the dominant amplitudes correspond to a frequency of runner rotational speed (f^*=1) and another frequency (f^*=13.6) of standing waves in the test rig. Low frequency stochastic noise is dominant at both 100% and 140% GVA in the draft tube. There are no amplitudes of deterministic frequency except the runner rotational speed at 140% GVA.

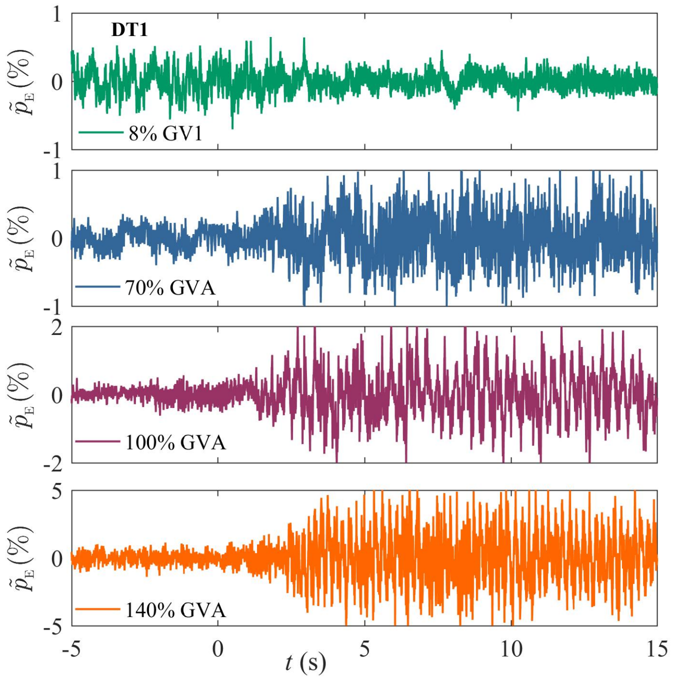

Figure 16 Extracted pressure fluctuations at DT1 in the draft tube during power ramp-down at 8%, 70%, 100% and 140% GVA. Location DT1 is can be seen in Figure 2; y-axis scale of the plots is different to visualize the pressure fluctuations. Time t=0 s indicates the start time of load change.

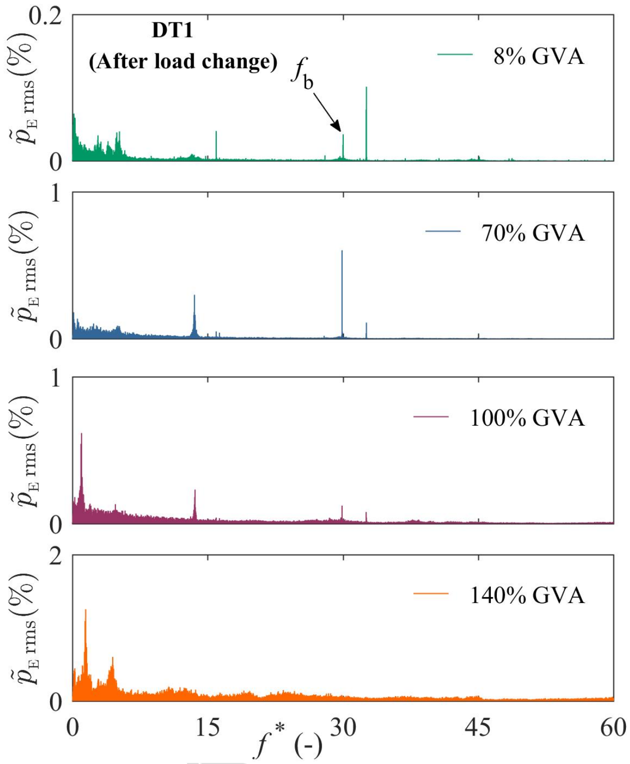

Figure 17 Spectral analysis of the pressure data acquired from DT1 at 8%, 70%, 100% and 140% GVA after the load change. The frequencies are normalized using Equation (11).

3.3 Stochastic frequencies

Overall analysis of the pressure data showed frequencies of stochastic component after the speed variation from the rated speed. It is natural that a turbine performs well at the rated speed and design load, and amplitudes of the deterministic frequencies, such as blade passing, runner rotational speed and vortex rope, are dominant. However, after the speed change, amplitudes of stochastic frequencies are expected due to deviation from the design load. In the current study, unlike other locations in the turbine, stochastic frequencies are dominant in the draft tube. There may not be gain (runner life) after changing the runner rotational speed, if the amplitudes of stochastic frequencies are dominant and induce dynamic stresses [11, 44, 53]. It is important to investigate the source of such fluctuations; e.g., are those fluctuations related to any specific flow condition, system vibration or the fluid-structure interaction? In this section, further analysis of the pressure data is presented, and the focus is to identify stochastic/deterministic frequencies at different locations in the turbine.

In the current study, the deterministic frequencies are RSI, runner rotational speed, vortex rope, standing waves, draft tube surging and vortex shedding from the guide vane/blade trailing edge. Another non-relevant deterministic frequency is the electrical interference from the DC generator/frequency convertor. The frequencies associated with the stochastic fluctuations may be associated with the hydro-mechanical interaction, system vibration and other random flow phenomena during speed variation. A signal-to-noise ratio (SNR) [50, 51] study is carried out for all cases of speed variation. Figure 18 shows signal-to-noise ratio in the pressure data before and after the load change. $\tilde{p}_E$=0.5 indicates the power of deterministic and stochastic frequencies is same at the measurement location. Pressure data before the load change shows that power of deterministic frequencies is dominant ($\tilde{p}_E \geq 0.5$), except DT1 for 8% and 140% GVA. After the load change, pressure data at DT1 shows very low power of the deterministic frequencies. High SNR values at VL1 for 70%, 100% and 140% GVA indicates the dominant signal power, which is associated with the amplitudes of blade passing frequency and the harmonics. Pressure data at R1 shows no significant change for all GVA, which may be due to mixed fluctuations of the guide passing frequency and the random fluctuations at that location.

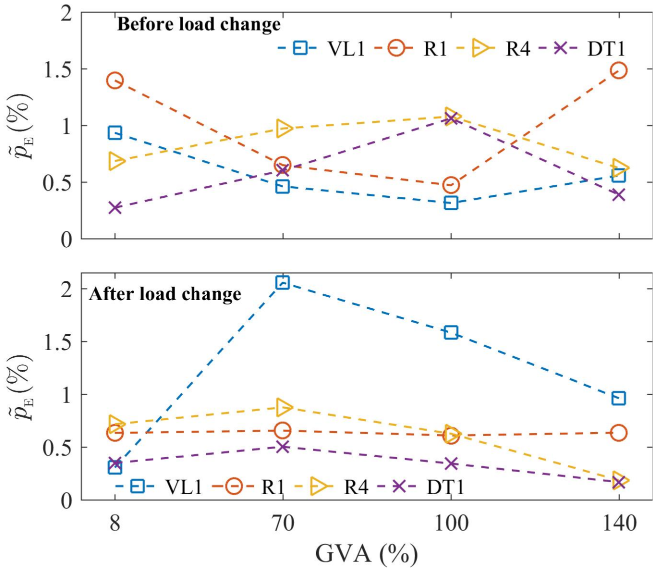

Figure 18 Signal-to-noise ratio in the acquired pressure data from VL1, R1, R4 and DT1 locations in the turbine.

In a hydraulic turbine, the pressure fluctuations are related to either local or global condition or both. Random flow phenomena, noise and vibration at specific location induce stochastic fluctuations, which are captured by the nearest pressure sensor. Vibration of a test rig at a particular frequency, RSI, standing waves and noise from the generator induce deterministic frequencies. Coherence and cross spectrum analysis [15, 50, 51, 54] is conducted to identify the frequencies, in-phase or out-of-phase, at different locations in the turbine. The in-phase frequencies indicate the same phenomena at different locations in the turbine. For example, four pressure sensors (R1, R2, R3 and R4) are located in the blade passage; a guide vane passing frequency propagates to the runner at the speed of sound that is captured by all sensors and the resulting coherence has unit value. The out-of-phase frequencies are associated with the phenomena occurring locally at different time. Figure 19 shows coherence in the pressure-time signals at 8% and 100% GVA after the load change. In the vaneless space, two pressure sensors were 120° circumferentially apart from each other. Due to geometrical combinations of blades and guide vanes, both sensors were experiencing the blade passing frequency (f_b) same time. Coherence between VL1 and VL2 for the blade passing frequency and harmonics is one. Both, 8% and 100%, GVA cases show frequencies less than 50 Hz with low coherence, which is random noise occurring locally at different time. In the runner, coherence between R1 and R2 at 100% GVA is well established and the deterministic, i.e., guide vane passing, frequency can be seen clearly. For 8% GVA, several peaks of different frequencies can be seen, which indicates the region around R1 and R2 experience nearly same flow condition in the blade passage. Analysis of R3 and R4 shows completely different coherence from that of the R1 and R2. Both deterministic and stochastic frequencies are in-phase at R3 and R4, including the low frequency noise. The source of both high and low frequency noise in the region between R3 and R4 may be the fluid-structure interaction, vibration of the runner (or from the DC generator/shaft), vortex shedding from the splitter trailing edge and influence from the draft tube. At 8% GVA, almost frequencies are in-phase, which is similar to that observed in the draft tube. Influence of the draft tube flow is strong at R3 and R4 locations. Coherence of all sensors located in the draft tube shows similar variation. At 8% GVA, a frequency spectrum is dominated by the stochastic frequencies. Unsteady vortex breakdown from the runner may be the source for such disturbing flow field. At 100% GVA, stochastic frequencies above 160 Hz are in-phase, except small variation between 260 and 300 Hz. To investigate the random fluctuations in the draft tube, cross spectrum analysis between DT1 and DT2 is carried out. The computed phase difference between the pressure fluctuations at DT1 and DT2 locations is shown in Figure 20. Figure 20(a) shows phase between DT1 and DT2 in radian. Low frequency fluctuations at DT2 location are almost 180° out-of-phase from that of the DT1, which agrees well with the coherence analysis shown in Figure 19. Such low frequency fluctuations may be associated with the vortex shedding from the blade/splitter trailing edge. Above 70 Hz, phase angle is almost zero, which indicates the existence of same frequency fluctuations at both locations in the draft tube cone. Further, arithmetic mean of DT1 and DT2 is computed (see Equation (13)), where the out-of-phase fluctuations occurring at exactly 180° will cancel out. Cross spectrum between DT1 and $\tilde{p}(t)_{\mathrm{m}}$ is investigated, which is shown in Figure 20(b). The result is quite different from that of DT1 and DT2. All remaining pressure fluctuations are in-phase with DT1, except 3.1 Hz which is related to runner rotational speed. To investigate the opposite behavior, pressure fluctuations at DT2 location are subtracted from the DT1 as shown in Equation (14) and cross spectrum analysis is carried out. The phase angle can be seen in Figure 20(c), where the frequencies from 160 Hz to 210 Hz are out-of-phase. Such high frequencies may be the result of coherent vortex structure in the draft tube cone and the vortex shedding from the blade/splitter trailing edge. There was no frequency related to the vortex rope at this GVA and operating load.

$$\tilde{p}(t)_m = \frac{\tilde{p}(t)_{\mathrm{DT1}} + \tilde{p}(t)_{\mathrm{DT2}}}{2} \quad \text{(Pa)} \tag{13}$$

$$\tilde{p}(t)_s = \tilde{p}(t)_{\mathrm{DT1}} - \tilde{p}(t)_{\mathrm{DT2}} \quad \text{(Pa)} \tag{14}$$

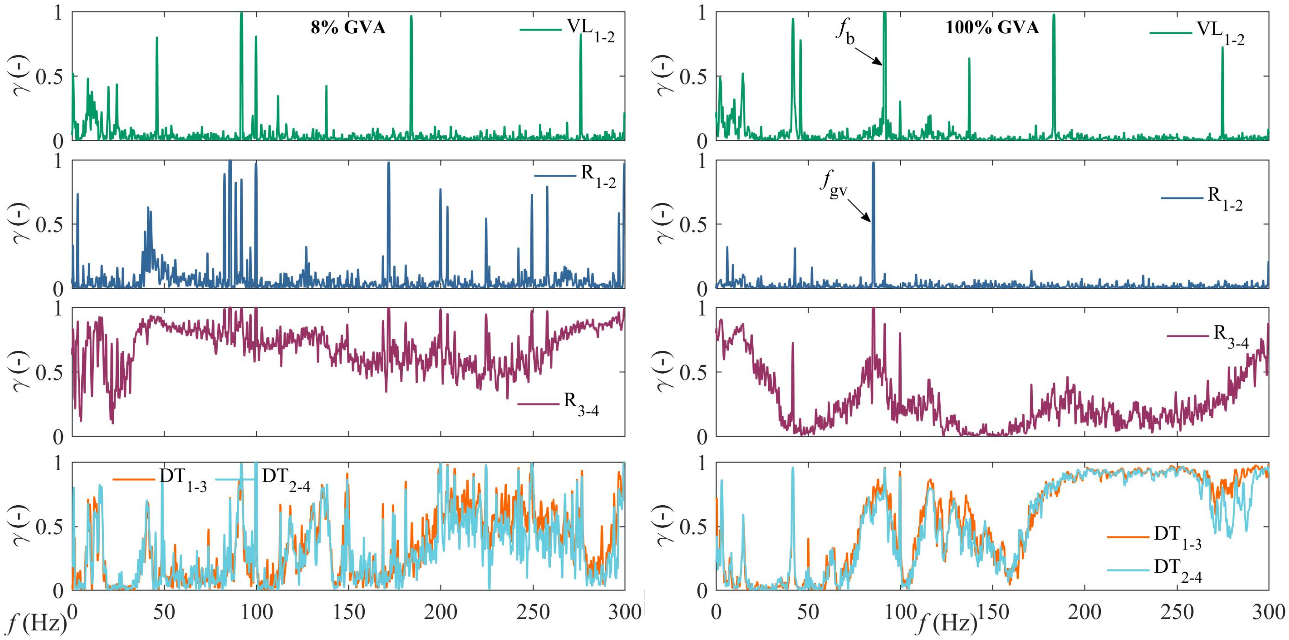

Figure 19 Coherence in pressure data acquired from different locations in the turbine at 8% GVA (left) and 100% GVA (right) during power ramp-down.

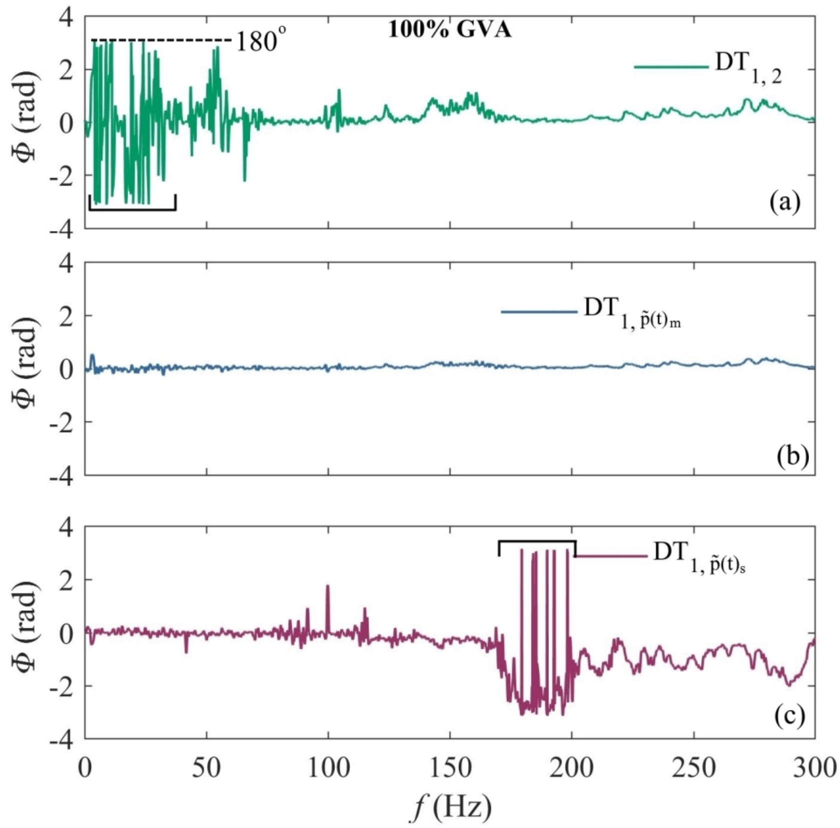

Figure 20 Cross spectrum analysis of DT1 and DT2 in the draft tube at 100% GVA during power ramp-down. Figure (a) shows phase between DT1 and DT2, figure (b) shows phase between DT1 and mean of DT1 and DT2, figure (c) shows phase between DT1 and difference of DT1 and DT2.

Time-dependent coherence between the runner pressure sensors, R1 and R4, is shown in Figure 21. We can see that only guide vane passing frequency is in phase all the time and the remaining frequencies are occurring at different time. This indicates the local flow conditions at R1 and R4 is completely different, except the RSI frequency. Pressure fluctuations at R4 location are strongly affected by the stochastic flow field in the draft tube cone. Pressure fluctuations at all locations in the draft tube were stochastic and no deterministic frequency was obtained except the blade passing frequency, which had similar amplitudes. To understand the draft tube flow and the corresponding frequency content in detail, a time-dependent spectral analysis is conducted at DT1 (see Figure 22). A deterministic frequency (f_b) is disappeared soon after the speed change. A frequency of 100 Hz corresponds to the electric current (50 Hz) induced by the DC generator and rectifier in the test rig. Time-dependent coherence between DT1 and DT2 at 8% GVA is shown in Figure 23. Before the load change, almost frequencies are in phase except low frequencies (<45 Hz). Pressure sensor DT1 was located at 180° circumferential position from the DT2 on the same plane. Pressure fluctuations at both locations are in-phase. Transition of coherence can be seen between 0 and 3 s. After t=3 s, the frequencies are out-of-phase, which indicates the local flow condition is dominant and no deterministic frequency associated with the global flow condition. In order to assess the ability of a machine to operate under variable-speed condition before fatigue damage will lead to cracking, a reasonable prediction method for the pressure loads is required. Due to the stochastic nature of the loads, an appropriate and efficient conversion of the dynamic pressure loads into deformations and further analysis is needed. In this turbine, stochastic pressure fluctuations were seen in the range of 10-50 Hz and 170-250 Hz. Majority of the fluctuations were associated to the local flow condition. In the runner, stochastic fluctuations were dominant at R3 and R4 locations, where the flow is strongly affected by the inter channel vortices and the draft tube. In the draft tube, change in combinations of flow velocities, tangential and axial, due to change of runner rotational speed, possibly resulted in strong vortex breakdown as well as flow separation. This may be investigated numerically and design optimized for the variable-speed operation.

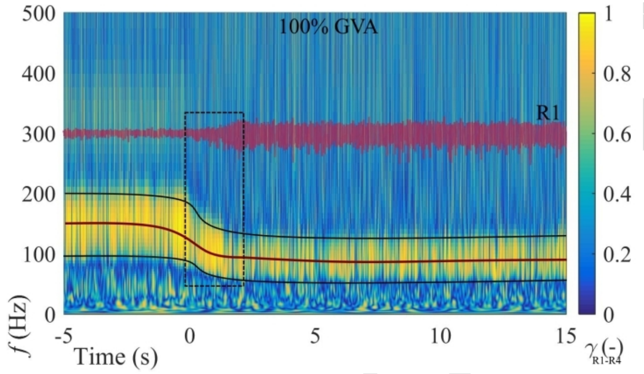

Figure 21 Coherence in pressure data acquired between R1 and R4 in the runner at 100% GVA during power ramp-down. Rectangular box of dash line indicates the time of power ramp-down. Pressure fluctuations (not scaled) at 300 Hz correspond to the location R1 to visualize the variation.

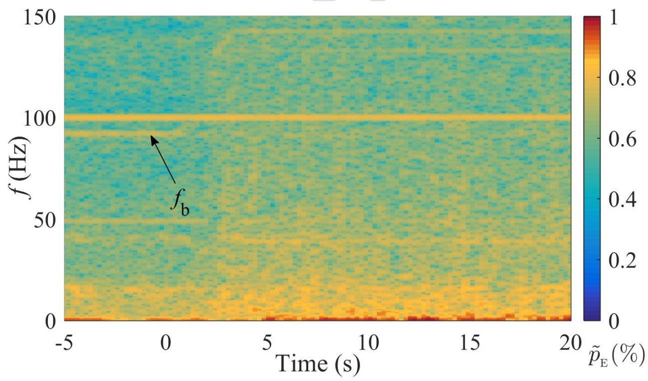

Figure 22 Spectral analysis of unsteady pressure fluctuations in the draft tube (locations DT1) during power ramp-up at 8% GVA. Time t=0 s indicates the start time of speed reduction.

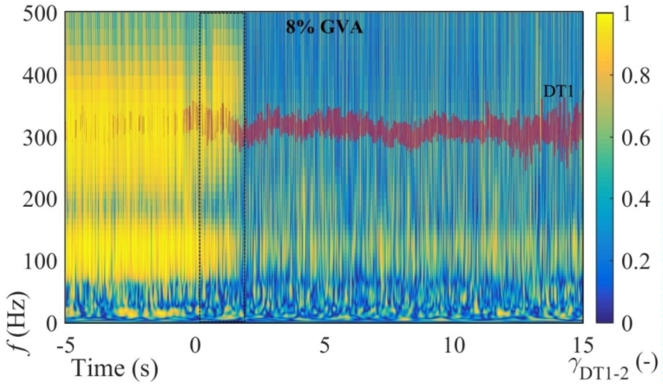

Figure 23 Coherence between DT1 and DT2 in the draft tube at 8% GVA during power ramp-up. Pressure fluctuations (not scaled) at 300 Hz correspond to the location DT1 to visualize the variation.

4. Conclusions

The present work was aimed to investigate the amplitudes of unsteady pressure fluctuations at different locations inside the turbine during speed variation and to investigate the change of pressure amplitudes with load. The speed variation was performed for 8%, 70%, 100% and 140% GVA. The runner rotational speed was changed by ±30% from the rated speed. To acquire unsteady pressure data, ten pressure sensors inside the turbine and two pressure sensors at the inlet conduit were flush mounted. In addition to the pressure data, torque, rotational speed, friction torque and net head were acquired during the measurements. Followings are the observations/findings based on current study:

- At constant GVA, shaft torque is inversely proportional to the runner rotational speed, and the change of output power is function of the rotational speed (ω). However, at 8% GVA, both shaft torque and power are inversely proportional to the rotational speed. Switching to the motor mode was observed when the hydraulic power was insufficient to meet the required hydraulic energy during the speed variation.
- Pressure at the turbine inlet was proportion to the speed change. As the speed was decreasing, discharge to the runner increased, hence the static pressure was dropped. Total pressure variation was 3-4% during the transients and the frequency of oscillations due to surging was 0.35 Hz, which was dampened after few seconds. The amplitudes of pressure fluctuations were 0.2-0.5% of ρE.

- Pressure in the vaneless space was linearly following the trend of runner rotational speed. The pressure amplitudes were increasing as the rotational speed deviates from the rated speed. The pressure amplitudes of deterministic frequencies were increased by 10-40% from the initial value, whereas the amplitudes of stochastic frequencies were increased by double. Interaction between the vortex shedding from the guide vanes and the blade stagnation point may be the source for high amplitudes of stochastic frequencies. The amplitudes may be strong enough to develop a fatigue in the prototype runner. This may be the topic of future study.
- Four pressure sensors (R1, R2, R3 and R4) in the runner provided quite useful information on how pressure amplitudes vary during speed variation. Pressure in the runner was linearly following the runner rotational speed, similar to the vaneless space. The pressure variation at R1 location was the maximum (up to 28%), and the amplitudes were up to 1.5% of ρE, which are 2 times the amplitudes at VL1. Unexpectedly, at 70% GVA, the blade passing frequency was obtained in the runner and the amplitudes were similar at all locations in the blade passage. The presence of blade passing frequency may be the result of hydro acoustic wave reflecting back from the guide vane wall.
- Pressure data analysis from the draft tube showed frequencies of both deterministic and stochastic pressure fluctuations with nearly same amplitudes after the speed variation. The amplitudes were 0.08%, 0.5%, 0.2%, and 1.3% of ρE at 8%, 70%, 100% and 140% GVA, respectively. Measurements at 70% GVA showed no vortex rope frequency after the speed change. However, the amplitudes of stochastic frequencies were increased. Similarly, at 140% GVA, amplitudes of stochastic frequencies were dominant, and no frequency of blade passing was obtained.
- During and after the speed variation, stochastic pressure fluctuations were dominant at certain locations in the turbine. The highest amplitudes of stochastic fluctuations were obtained at 8% and 140% GVA. The amplitudes after the load change were increased by two times than that of the before load change. The stochastic and deterministic pressure fluctuations at R1 location were constant for all operating conditions after the load change. This indicates the variation of

load/discharge has negligible effect on the runner flow field. Moreover, the stochastic pressure fluctuations were dominant in the draft tube, particularly frequencies less than 50 Hz, and the amplitudes were similar to those of the RSI frequencies. Cross spectrum analysis, showed that the stochastic type pressure fluctuations were out-of-phase after the load change reduction from BEP. Variation of runner angular speed may not give benefit in terms of fatigue loading to the blades when the stochastic pressure fluctuations are persisting. Unsteady pressure measurements under such conditions are important (even if the hydraulic efficiency is better than the expected) to identify the stable operating regions, where the stochastic and deterministic (RSI and vortex rope frequencies) pressure amplitudes are minimum.

- Two different approaches are generally applied while implementing the variable-speed technology in hydraulic turbines: (1) introduce in the existing turbine with minor upgrade into generating system and (2) a completely new design. The current investigation addresses both aspects. For the case (1), while changing rotational speed of the runner from the rated speed, amplitudes of stochastic frequencies increase significantly in the runner and draft tube. The speed change beyond ±25% of the rated speed may not be advantageous due to the presence strong amplitudes associated with the random flow phenomena. For the case (2) of new design implementation, reliable estimation of the stochastic pressure fluctuations at the blade trailing edge is important. The runner design should be balanced between the efficiency requirement and the induced fatigue loading otherwise there may not be the benefit of variable-speed technology in terms of runner life as compared to the synchronous speed machines.

5. Future work

Numerically investigate the flow field inside the turbine during these transient conditions, particularly vaneless space and blade passages. Future study will focus in further investigations of stochastic pressure fluctuations using different techniques, such as rainflow diagram and the time-dependent techniques. The study will also focus on the stochastic fluctuations and the impact on runner life considering over 25 load variation cycles per day.

Acknowledgments

The experimental studies were conducted under a research project "HiFrancis." The project was financially supported by The Research Council of Norway and the Norwegian hydropower industries.

Nomenclatures

Abbreviations

BEP	Best efficiency point
DT1, DT2, DT3, DT4	Locations of pressure sensors in the draft tube
GVA	Guide vane aperture
IN1, IN2	Locations of the pressure sensors on the conduit
NTNU	Norwegian University of Science and Technology
R1, R2, R3, R4	Locations of pressure sensors in the runner
RSI	Rotor-stator interaction
SNL	Speed-no-load
SNR	Signal-to-noise ratio
VL1, VL2	Locations of pressure sensors in the vaneless space

Variables

D	Diameter (m)
E	Specific hydraulic energy (J kg^{-1}); $E=gH$
$\hat{e}$	Uncertainty (%)
f	Frequency (Hz); $f^{*}=f/n$
g	Gravity (m s^{-2}); g = 9.821465 m s^{-2}
H	Head (m)
J	Polar moment of inertia (kg m^{2})
n	Runner angular speed (rev s^{-1})
n_{ED}	Speed factor (-)
P	Power (W)
p	Pressure (Pa)
$\tilde{p}_E$	Factor of pressure fluctuations (-); $\tilde{p}_E=\tilde{p}/\rho E$
Q	Discharge (m^{3} s^{-1})
Q_{ED}	Discharge factor (-)
T	Torque (N m)
t	Time (s)
x	Variable
z	Number of blades/guide vanes

Greek letters

η	Efficiency (-)
ρ	Water density (kg m^{-3})
α	Guide vane angle (°)
γ	Coherence (-)
ω	Angular speed (rad s^{-1})

Subscripts

b	Blade

gv Guide vane
h Hydraulic
m Mechanical
r Relative
rh Rheingans frequency/ vortex rope frequency
s Systematic
t Total

References

[1] Claude, J.-M., "Performances Achieved to the Grid by a Full Power Converter Used in a Variable Speed Pumped Storage Plant," Proc. HYPERBOLE, Porto, Portugal, p. 6.

[2] Chazarraa, M., Pérez-Díaza, J., and García-Gonzálezb, J., "Economic Viability of Pumped-Storage Power Plants Equipped with Ternary Units and Considering Hydraulic Short-Circuit Operation," Proc. HYPERBOLE, Porto, Portugal, p. 5.

[3] Gjengedal, T., "Integration of Wind Power and the Impact on Power System Operation," Proc. Power Engineering, 2003 Large Engineering Systems Conference on, IEEE, pp. 76-83. http://dx.doi.org/10.1109/LESCPE.2003.1204683.

[4] Caralis, G., Papantonis, D., and Zervos, A., 2012, "The Role of Pumped Storage Systems Towards the Large Scale Wind Integration in the Greek Power Supply System," Renewable & Sustainable Energy Reviews, **16**(5), pp. 2558-2565. http://dx.doi.org/10.1016/j.rser.2012.01.068.

[5] Bessa, R., Moreira, C., Silva, B., Filipe, J., and Fulgêncio, N., "Role of Pump Hydro in Electric Power Systems," Proc. HYPERBOLE, Porto, Portugal, p. 7.

[6] Trivedi, C., Gandhi, B., and Cervantes, M., 2013, "Effect of Transients on Francis Turbine Runner Life: A Review," Journal of Hydraulic Research, **51**(2), pp. 121-132. http://dx.doi.org/10.1080/00221686.2012.732971.

[7] Ulbig, A., Rinke, T., Chatzivasileiadis, S., and Andersson, G., 2013, "Predictive Control for Real-Time Frequency Regulation and Rotational Inertia Provision in Power Systems," Ieee Decis Contr P, pp. 2946-2953. http://dx.doi.org/10.1109/CDC.2013.6760331.

[8] Yang, W. J., Norrlund, P., Saarinen, L., Yang, J. D., Guo, W. C., and Zeng, W., 2016, "Wear and Tear on Hydro Power Turbines - Influence from Primary Frequency Control," Renewable Energy, **87**, pp. 88-95. http://dx.doi.org/10.1016/j.renene.2015.10.009.

[9] Hell, J., "High Flexible Hydropower Generation Concepts for Future Grids," Proc. HYPERBOLE, Porto, Portugal, p. 7.

[10] Trivedi, C., Cervantes, M., Dahlhaug, O., and Gandhi, B., 2015, "Experimental Investigation of a High Head Francis Turbine During Spin-No-Load Operation," Journal of Fluids Engineering, **137**(6), p. 061106. http://dx.doi.org/10.1115/1.4029729.

[11] Nennemann, B., Morissette, J. F., Chamberland-Lauzon, J., Monette, C., Braun, O., Melot, M., Coutu, A., Nicolle, J., and Giroux, A. M., "Challenges in Dynamic Pressure and Stress Predictions at No-Load Operation in Hydraulic Turbines," Proc. 27th IAHR Symposium Hydraulic Machinery and systems, Montreal, Canada, p. 10. http://dx.doi.org/10.1088/1755-1315/22/3/032055.

[12] Mende, C., Weber, W., and Seidel, U., 2016, "Progress in Load Prediction for Speed-No-Load Operation in Francis Turbines," IOP Conference Series: Earth and Environmental Science, **49**(6), p. 062017. http://dx.doi.org/10.1088/1755-1315/49/6/062017.

[13] Zeng, W., Yang, J., and Yang, W., 2016, "Instability Analysis of Pumped-Storage Stations under No-Load Conditions Using a Parameter-Varying Model," Renewable Energy, **90**, pp. 420-429. http://dx.doi.org/10.1016/j.renene.2016.01.024.

[14] Ellingsen, R., and Storli, P.-T., 2015, "Simulations of the Dynamic Load in a Francis Runner Based on Measurements of Grid Frequency Variations," International Journal of Fluid Machinery and Systems, **8**(2), pp. 102-112. http://dx.doi.org/10.5293/ijfms.2015.8.2.102.

[15] Dörfler, P., Sick, M., and Coutu, A., 2013, Flow-Induced Pulsation and Vibration in Hydroelectric Machinery, Springer-Verlag, London. http://dx.doi.org/10.1007/978-1-4471-4252-2.

[16] Magnoli, M. V., and Maiwald, M., "Influence of Hydraulic Design on Stability and on Pressure Pulsations in Francis Turbines at Overload, Part Load and Deep Part Load Based on Numerical Simulations and Experimental Model Test Results," Proc. 27th IAHR Symposium Hydraulic Machinery and systems, Montreal, Canada, pp. 1-8. http://dx.doi.org/10.1088/1755-1315/22/3/032013.

[17] Keck, H., Weiss, T., Michler, W., and Sick, M., 2009, "Recent Developments in the Dynamic Analysis of Water Turbines," Proceedings of the Institution of Mechanical Engineers, Part A: Journal of Power and Energy, **223**(4), pp. 415-427. http://dx.doi.org/10.1243/09576509JPE578.

[18] Seidel, U., Mende, C., Hübner, B., Weber, W., and Otto, A., "Dynamic Loads in Francis Runners and Their Impact on Fatigue Life," Proc. IOP Conference Series: Earth and Environmental Science, Montreal, Canada, p. 9. http://dx.doi.org/10.1088/1755-1315/22/3/032054.

[19] Nishi, M., and Liu, S., 2013, "An Outlook on the Draft-Tube-Surge Study," International Journal of Fluid Machinery and Systems, **6**(1), pp. 33-48. http://dx.doi.org/10.5293/ijfms.2013.6.1.033.

[20] Shingai, K., Okamoto, N., Tamura, Y., and Tani, K., 2014, "Long-Period Pressure Pulsation Estimated in Numerical Simulations for Excessive Flow Rate Condition of Francis Turbine," Journal of Fluids Engineering, **136**(7), p. 071105. http://dx.doi.org/10.1115/1.4026584.

[21] Chen, T., and Li, S. C., 2011, "Numerical Investigation of Guide-Plate Induced Pressure Fluctuations on Guide Vanes of Three Gorges Turbines," Journal of Fluids Engineering, **133**(6), p. 061101. http://dx.doi.org/10.1115/1.4004257.

[22] Liu, X., Luo, Y., Karney, B. W., and Wang, W., 2015, "A Selected Literature Review of Efficiency Improvements in Hydraulic Turbines," Renewable and Sustainable Energy Reviews, **51**, pp. 18-28. http://dx.doi.org/10.1016/j.rser.2015.06.023.

[23] Beevers, D., Branchini, L., Orlandini, V., De Pascale, A., and Perez-Blanco, H., 2015, "Pumped Hydro Storage Plants with Improved Operational Flexibility Using Constant Speed Francis Runners," Applied Energy, **137**, pp. 629-637. http://dx.doi.org/10.1016/j.apenergy.2014.09.065.

[24] Monette, C., Marmont, H., Chamberland-Lauzon, J., Skagerstrand, A., Coutu, A., and Carlevi, J., "Cost of Enlarged Operating Zone for an Existing Francis Runner," Proc. 28th IAHR Symposium on Hydraulic Machinery and Systems, Grenoble, France, IAHR. http://dx.doi.org/10.1088/1755-1315/49/7/072018.

[25] Magnoli, M. V., 2014, "Numerical Simulation of Pressure Oscillations in Large Francis Turbines at Partial and Full Load Operating Conditions and Their Effects on the Runner Structural Behaviour and Fatigue Life,"Ph. D., Technische Universitat Munchen.

[26] Farell, C., Arroyave, J., Cruz, N., and Gulliver, J., 1983, "Hydrodynamics of Variable Speed Turbines," University of Minnesota, Minnesota, USA.

[27] Farell, C., and Gulliver, J., 1987, "Hydromechanics of Variable Speed Turbines," Journal of Energy Engineering, **113**(1), pp. 1-13. http://dx.doi.org/10.1061/(asce)0733-9402(1987)113:1(1).

[28] Sivakumar, N., Das, D., and Padhy, N. P., 2014, "Variable Speed Operation of Reversible Pump-Turbines at Kadamparai Pumped Storage Plant – a Case Study," Energy Conversion and Management, **78**, pp. 96-104. http://dx.doi.org/10.1016/j.enconman.2013.10.048.

[29] Trivedi, C., Gandhi, B., Cervantes, M., and Dahlhaug, O., 2015, "Experimental Investigations of a Model Francis Turbine During Shutdown at Synchronous Speed," Renewable Energy, **83**, pp. 828-836. http://dx.doi.org/10.1016/j.renene.2015.05.026.

[30] Trivedi, C., Cervantes, M., Gandhi, B., and Dahlhaug, O., 2014, "Pressure Measurements on a High-Head Francis Turbine During Load Acceptance and Rejection," Journal of Hydraulic Research, **52**(2), pp. 283-297. http://dx.doi.org/10.1080/00221686.2013.854846.

[31] Trivedi, C., Cervantes, M., Gandhi, B., and Dahlhaug, O., 2014, "Transient Pressure Measurements on a High Head Model Francis Turbine During Emergency Shutdown, Total Load Rejection, and Runaway," Journal of Fluids Engineering, **136**(12), p. 121107. http://dx.doi.org/10.1115/1.4027794.

[32] Trivedi, C., Cervantes, M., Gandhi, B., and Dahlhaug, O., 2014, "Experimental Investigations of Transient Pressure Variations in a High Head Model Francis Turbine During Start-up and Shutdown," Journal of Hydrodynamics, Ser. B, **26**(2), pp. 277-290. http://dx.doi.org/10.1016/S1001-6058(14)60031-7.

[33] Hosseinimanesh, H., Devals, C., Nennemann, B., Reggio, M., and Guibault, F., 2016, "A Numerical Study of Francis Turbine Operation at No-Load Condition," Journal of Fluids Engineering, **139**(1), p. 011104. http://dx.doi.org/10.1115/1.4034422.

[34] Widmer, C., Staubli, T., and Ledergerber, N., 2011, "Unstable Characteristics and Rotating Stall in Turbine Brake Operation of Pump-Turbines," Journal of Fluids Engineering, **133**(4), p. 041101. http://dx.doi.org/10.1115/1.4003874.

[35] Trivedi, C., Cervantes, M. J., and Gandhi, B. K., 2016, "Numerical Investigation and Validation of a Francis Turbine at Runaway Operating Conditions," Energies, **9**(3), p. 22. http://dx.doi.org/10.3390/en9030149.

[36] Zuo, Z., Liu, S., Sun, Y., and Wu, Y., 2015, "Pressure Fluctuations in the Vaneless Space of High-Head Pump-Turbines-a Review," Renewable and Sustainable Energy Reviews, **41**(0), pp. 965-974. http://dx.doi.org/10.1016/j.rser.2014.09.011.

[37] Liu, X., Luo, Y., and Wang, Z., 2016, "A Review on Fatigue Damage Mechanism in Hydro Turbines," Renewable and Sustainable Energy Reviews, **54**, pp. 1-14. http://dx.doi.org/10.1016/j.rser.2015.09.025.

[38] Trivedi, C., and Cervantes, M., 2017, "Fluid Structure Interaction in Hydraulic Turbines: A Perspective Review," Renewable & Sustainable Energy Reviews, **68**(1), pp. 87-101. http://dx.doi.org/10.1016/j.rser.2016.09.121.

[39] Hübner, B., Weber, W., and Seidel, U., "The Role of Fluid-Structure Interaction for Safety and Life Time Prediction in Hydraulic Machinery," Proc. 28th IAHR Symposium on Hydraulic Machinery and System, Grenoble, France, IAHR. http://dx.doi.org/10.1088/1755-1315/49/7/072007.

[40] Coutu, A., Roy, M. D., Monette, C., and Nennemann, B., "Experience with Rotor-Stator Interactions in High Head Francis Runner," Proc. Proceedings of 24th IAHR symposium on hydraulic machinery and systems, Foz do Iguassu, Brazil, p. 10.

[41] Trivedi, C., 2017, "A Review on Fluid Structure Interaction in Hydraulic Turbines: A Focus on Hydrodynamic Damping," Engineering Failure Analysis, **77**, pp. 1-22. http://dx.doi.org/10.1016/j.engfailanal.2017.02.021.

[42] Heckelsmueller, G. P., 2015, "Application of Variable Speed Operation on Francis Turbines," Ingeniería e Investigación, **35**(1), p. 5. http://dx.doi.org/10.15446/ing.investig.v35n1.44995.

[43] Béguin, A., Nicolet, C., Hell, J., and Moreira, C., "Assessment of Power Step Performances of Variable Speed Pump-Turbine Unit by Means of Hydro-Electrical System Simulation," Proc. HYPERBOLE, Porto, Portugal, p. 5.

[44] Morissette, J., Chamberland-Lauzon, J., Nennemann, B., Monette, C., Giroux, A., Coutu, A., and Nicolle, J., "Stress Predictions in a Francis Turbine at No-Load Operating Regime," Proc. 28th IAHR Symposium on Hydraulic Machinery and Systems, Grenoble, France, IAHR. http://dx.doi.org/10.1088/1755-1315/49/7/072016.

[45] Trivedi, C., 2015, "Investigations of Transient Pressure Loading on a High Head Francis Turbine,"Ph. D., Luleå University of Technology, Luleå. http://dx.doi.org/10.13140/2.1.4087.2006.

[46] IEC 60193, 1999, "Hydraulic Turbines, Storage Pumps and Pump-Turbines: Model Acceptance Tests," International standard, International Electrotechnical Commission, 3, rue de Varembé, PO Box 131, CH-1211 Geneva 20, Switzerland. 16 November, p. 578.

[47] Trivedi, C., Cervantes, M., Gandhi, B., and Dahlhaug, O. G., 2013, "Experimental and Numerical Studies for a High Head Francis Turbine at Several Operating Points," Journal of Fluids Engineering, **135**(11), pp. 1111021-1111017. http://dx.doi.org/10.1115/1.4024805.

[48] Trivedi, C., 2014, "Experimental and Numerical Investigations on Steady State and Transient Characteristics of a High Head Model Francis Turbine,"Ph. D., Indian Institute of Technology, Roorkee.

[49] Trivedi, C., 2013, "Transients in High Head Francis Turbines,"Licentiate, Luleå University of Technology, Luleå. http://dx.doi.org/10.13140/2.1.1482.5764.

[50] Dolecek, G. J., 2013, Random Signals and Processes Primer with Matlab, Springer New York. http://dx.doi.org/10.1007/978-1-4614-2386-7.

[51] O'Shea, P., Sadik, A. Z., and Hussain, Z. M., 2011, Digital Signal Processing an Introduction with Matlab and Applications, Springer Berlin Heidelberg. http://dx.doi.org/10.1007/978-3-642-15591-8.

[52] Trivedi, C., Cervantes, M. J., and Dahlhaug, O. G., 2016, "Numerical Techniques Applied to Hydraulic Turbines: A Perspective Review," Applied Mechanics Reviews, **68**(1), p. 29. http://dx.doi.org/10.1115/1.4032681.

[53] Melot, M., Monette, C., Coutu, A., and Nenneman, B., "Speed-No-Load Operating Condition: A New Standard Francis Runner Design Procedure to Predict Static Stresses," Proc. Hydro 2013, Innsbruck, Austria, p. 8.

[54] Doerfler, P., and Ruchonnet, N., "A Statistical Method for Draft Tube Pressure Pulsation Analysis," Proc. IOP Conference Series: Earth and Environmental Science, 26th IAHR Symposium on Hydraulic Machinery and Systems, IOP Publishing, p. 062002. http://dx.doi.org/10.1088/1755-1315/15/6/062002.

Highlights

- Time-dependent pressure amplitudes during speed variation were investigated.
- Pressure amplitudes in the runner are strongly coupled with the runner speed.
- Stochastic frequencies are dominant at the runner outlet and draft tube.
- Variable-speed configuration allows stable power generation at off-design.
- Proper analysis of pressure fluctuations across the operating range is vital.